Substrate Effect on the High-Temperature Oxidation Behavior of a Pt-Modified Aluminide Coating. Part I: Influence of the Initial Chemical Composition of the Coating Surface

Nadia Vialas, Daniel Monceau

Substrate Effect on the High-Temperature Oxidation Behavior of a Pt-Modified Aluminide Coating. Part I: Influence of the Initial Chemical Composition of the Coating Surface

Nadia Vialas* and Daniel Monceau*†

The effect of substrate composition on the oxidation behavior of the industrial NiPtAl coating RT22™ was investigated by studying the isothermal and cyclic-oxidation behavior of this coating deposited on three different Ni-base superalloys (CMSX-4™, SCB™ and IN792™). Isothermal tests were performed at 900, 1050 and 1150°C for 100 h. Cyclic oxidation was studied at 900°C with a holding time of 300 h for up to 52 cycles (i.e, 15,600 h at 900°C). Thermogravimetric analysis (TGA), X-ray diffraction (XRD), microstructural and analytical investigations using scanning-electron microscopy (SEM) and transmission-electron microscopy (TEM), both equipped with energy-dispersive X-ray spectroscopy (EDS) were performed to characterize the oxidation behavior of the systems studied. An effect of the superalloy substrate was observed and related to the initial chemical composition of the coating surface which depends on the superalloy and the associated heat treatments. The effect of the substrate's alloying elements is discussed. Particularly the influence of Ti and Ta that formed rutile-type oxides inducing oxide-scale cracking and spallation. The excellent resistance to cyclic oxidation of the coating systems studied at 900°C was also demonstrated from very long duration tests of 15,600 h.

KEY WORDS: Pt-modified aluminide coating; Ni-base superalloy; high-temperature oxidation; long-term cyclic oxidation; alloying elements; RT22™; IN792™; CMSX-4™; SCB™

*CIRIMAT UMR 5085, ENSIACET-INPT, 31077, Toulouse Cedex 4, France.
E-mail: Daniel.Monceau@ensiacet.fr

INTRODUCTION

Improving gas-turbine performances requires to identify and understand the damaging processes occurring during their service life. This is particularly important for gas-turbine blades which are subjected to high temperature and aggressive oxidizing environments. Platinum-modified aluminide coatings are widely used to protect Ni-base superalloys for aero and industrial gas-turbine blades.[1] Therefore, a better understanding and analysis of the behavior and performance of these coatings is useful, and the present work was devoted to the oxidation behavior of the industrial diffusion coating RT22™. For a diffusion coating, the first parameter to consider is the coating composition and its microstructure which is affected by the superalloy substrate during application of the coating and the associated heat treatments, as well as during the service life at high temperature. Indeed, substrate alloying elements can be found in solid solution in the coating or inside precipitate.[2–4]

A number of previous papers have studied the oxidation of bulk nickel-aluminide and aluminide coatings. In the early stage of oxidation of nickel-auminide diffusion coatings, stable oxides such as α-Al_2O_3 or TiO_2 (when Ti is present), and transient oxides such as γ-Al_2O_3, δ-Al_2O_3 and θ-Al_2O_3 are formed. When the temperature dwell is extended, transient alumina transforms to α-Al_2O_3, starting at the metal/oxide interface, to form a continuous and protective oxide-scale layer. Whereas α-Al_2O_3 is the moss-stable phase, its thermodynamic stability is only slightly higher than the stability of the other Al_2O_3 phases, and the phase transformation may take a long time, especially at lower temperatures. Moreover, when cyclic oxidation is considered, one has to take into account that transient alumina can re-form on the bare-metal surface left by oxide-scale spalling at the metal/oxide interface. It is generally admitted that the relatively fast-growing theta- and delta-alumina phases with a whisker-like or platelet-like morphology are growing by cationic diffusion, although it is difficult to prove[5] since the transition alumina phase is difficult to isolate. The bulk diffusion of O and Al in α-Al_2O_3 single crystals is very slow, and the growth of α-Al_2O_3 scale is controlled by grain-boundary diffusion when the grains are small enough. Moreover, a strong correlation exists between roughness and oxide grain size.[6] The growth mechanism of Al_2O_3 scales is expected to depend strongly on the chemical composition of the aluminide coating.[7] Impurities and dopants affect the transport properties of α-Al_2O_3 which is an extrinsic semiconductor, they modify the grain size and sintering, and influence also the transient-to-alpha-alumina transformation.[8] Then, the effects of dopants and impurities on the oxidation kinetics are complex, although often observed.[9] Schumann *et al.*[10] reported an anionic growth of α-Al_2O_3 on

NiAl at 1200°C, but at the same temperature, Pint *et al.*[11] have shown that Y and Zr dopants changed the scale-growth mechanism from a mixed Al and O transport to predominantly O transport when alpha alumina is formed. Young *et al.*[12] observed a cationic growth on Y- and Zr-doped β-NiAl, but this could be due to the presence of transient alumina as suggested by Pint *et al.*[11] Ti, which is present in the three substrate alloys studied here, is known to accelerate the transient-to-alpha-alumina transformation.[8] This recent observation can be linked to the fact that NiAl with a dispersion of TiO_2 quickly forms an α-Al_2O_3 scale.[13] During their service life, gas-turbine blades are submitted to thermal cycling inducing the spallation of the protective α-Al_2O_3 scale and an increase in Al consumption. Oxide-scale-spallation results from the combination of several parameters and processes such as energy of metal/oxide interface, growth and thermal stresses,[14] surface roughness, surface preparation,[15] temperature, temperature drop, cycle frequency[16,17] and is also dependent on material composition[18] and microstructure.

Modifications of coating composition and microstructure result from the combination of high-temperature oxidation-corrosion and of interdiffusion between the coating and its substrate. Several author[4,19] have shown that Ti diffuses quickly through the coating and becomes incorporated into the oxide scale by forming a TiO_2 layer on the top of the Al_2O_3 scale. In the same way, Ta-rich oxides could be formed.[19] Such Ti, Ta-rich oxides formation could accelerate the growth kinetics of oxide scales[20] and promote oxide-scale cracking.[4,19–23] All these observations indicate that the durability of a superalloy/coating system depends not only on the nominal coating composition and microstructure but also on the substrate composition and of the preparation process and subsequent heat-treatment. Therefore, any modelling of the properties and behavior of a coating must be based on the characterization of the whole coating/substrate system.

In the present study, the same industrial platinum-modified aluminide RT22™ coating was deposited on three different Ni-base superalloys: CMSX-4™, SCB™ and IN792™. In this first part of the paper, the as-coated microstructures are described and the effects of the substrate on the scale-growth kinetics and on the oxide-scale morphology, microstructure and composition are reported. Results concerning the short-term isothermal oxidation at 900, 1050 and 115°C and the long-term, cyclic-oxidation tests (up to 15,600 h) at 900°C are discussed. The effect of substrate alloying elements Ti and Ta is more particularly detailed. This first part of the study focuses on the influence of the substrate on the composition and microstructure of the Pt-modified-aluminide coating. The kinetics and long-term consequences of Al consumption by selective oxidation, scale spallation and interdiffusion will be discussed in a second

part which presents long-term cyclic oxidation tests performed at higher temperature (1050°C).

EXPERIMENTAL PROCEDURE

Materials

Three nickel-base superalloys were used as substrates: two single-crystal nickel-base superalloys, CMSX-4^{TM} and SCB^{TM}, and a polycrystalline nickel-base superalloy IN792^{TM}. The nominal chemical compositions of the investigated substrates are reported in Table I. Single-crystal CMSX-4^{TM} is a second-generation Re-containing superalloy. Single-crystal SCB was developed by ONERA within the framework of a European program.[24] Cast polycrystalline IN792^{TM} was provided by Turbomeca-SAFRAN and contains 0.5 wt% of Hf. All the specimens were discs of 9 mm in diameter and 2 mm thickness. They were all coated with the industrial coating RT22^{TM} manufactured by Chromalloy France. The RT22^{TM} diffusion coating is a high-activity, platinum-modified aluminide. After alumina grit blasting and cleaning of the substrates, Pt was electrolytically deposited onto disc specimens. The geometry and size of test specimens used for thermogravimetry analysis required to laser weld a small lateral rod of IN82^{TM} for the electrical contact required by the electrolytic deposition process of Pt. The thickness of Pt deposits is 7 ± 2 μm. After Pt deposition, diffusion treatments were performed under high vacuum ($P < 10^{-3}$ Pa). The heat-treatment temperature and duration depend on the superalloy, 1 h at 1010°C for single-crystal superalloys CMSX-4^{TM} and SCB^{TM} and 2 h at 1010°C for polycrystalline superalloy IN792^{TM}. Aluminizing was then realized by pack cementation at 996°C. Finally, post-coating heat treatments were performed depending on superalloy substrate as reported in Table II.

The above procedure lead to a total coating thickness of 75 ± 7 μm on the three investigated substrates. As shown by the surface roughness measured with an optical microscope equipped with a Zigo-newview^{TM}-100 interferometer and reported in Table II, no significant influence of substrate on surface roughness was detected. All as-processed coatings are rather rough with an irregular surface when compared with aluminide CVD

Table I. Nominal Atomic Composition of CMSX-4, SCB and 1N792 Substrates

%at	Ni	Cr	Co	Al	Ti	Ta	W	Mo	Re	Hf	Zr	Fe	Si
CMSX-4	63	7.5	10	12.6	1.3	2.2	2.1	0.3	1	0.03	0.005		
SCB	66	13	5	8.5	5.5	0.6	1.2	0.6					
IN792	60.1	13.5	9	7.6	5	1.3	1.2	1.2		0.2	0.1	0.5	0.4

Table II. Post-Coating Heat Treatments Depending on Superalloy Substrate

	CMSX-4	SCB	IN792
Solution heat treatment	2 h at 1120°C ± 10°C	None	2 h at 1120°C ± 10°C
1st ageing	20 h at 870°C	24 h at 850°C	24 h at 845°C ± 10°C
2nd ageing	None	None	16 h at 760°C ± 10°C
R_a(μm)	1.3	1.5	1.3

Coating surface roughness in terms of parameter R_a.

coatings with a R_a of about 0.5 μm (R_a is the average of distance between the surface and the virtual mean flat surface). But they are less rough that VPS NiCoCrAlY coatings (typical R_a of about 5 or 6 μm).

Experimental Methods

As-processed coated specimens were oxidized isothermally and cyclically. No additional polishing of coated specimens, was performed before oxidation tests to reproduce as well as possible the normal service conditions. Samples were only cleaned in ultrasonic baths with acetone and ethanol before oxidation tests. Isothermal-oxidation tests were performed using a symmetrical Setaram TGA24S thermobalance for 100 h in flowing synthetic air at 900, 1050 and 1150°C, with a heating rate of 60°C/min. Mass gains recorded during specimen heating were not taken into account. Mass-gain curves were analyzed by local fitting to a general parabolic law[25] which permits to detect and analyze the variations of the parabolic rate constant k_p as a function of time. All sample surfaces and cross-sections were examined by SEM.

Long-term cycles (holding time of 300 h) were performed up to 52 cycles (i.e., 15,600 h) at 900°C in still laboratory air in a Carbolite™ furnace. Pt/Pt–Ph thermocouples (0.2 mm in diameter) were spot welded on spare samples to draw a thermal map of the furnace and to measure heating and cooling rates of test specimens. Specimens were hung with a platinum wire on alumina rods and placed on a sample-holder in the hot furnace. The measured heating rate was 3°C/s. Each cycle consisted of 300 h of heating at 900°C, then all specimens were maintained for 300 h in the furnace at 900 ± 3°C, then removed from the furnace and cooled to room temperature in front of fans. This procedure leads to an initial cooling rate of 9°C/s. Before testing and after cycle, specimens were weighted with an accuracy of 10μg by using a Sartorius™ microbalance Genius ME215S. The Net Mass Change per unit area (NMC) was measured as a function of cycle number, spalled-oxide mass was not included in NMC measurements. Three samples for each system were initially placed in the furnace, so that the

microstructure of one specimen of each coating system studied was investigated after 6, 17 and 35 cycles of 300 h at 900°C.[26]

All sample surfaces and cross-sections were examined before and after oxidation by using a Leo^{TM}435 scanning-electron microscope (SEM) equipped with a PGT^{TM} energy-dispersive X-ray spectrometry system (EDS). Oxidized samples were coated with Ni before molding. Furthermore, thin cross sections of oxide scales were prepared and examined in Jeol^{TM} 2010 TEM, equipped with a Voyager EDS system. TEM samples were prepared as follow. Two oxidized parallelepiped pieces were cut with a wire diamond saw. The pieces were glued together, oxide next to the oxide, and embedded in a 3 mm brass tube using a Gatan epoxy resin. After curing, the tube was sectioned into 300 μm-thick discs which were mechanically polished on the two faces and dimpled with a South Bay Technology dimpler. Finally, they were ion-milled during several hours using a Gatan Precision Ion Polishing System until a hole could be detected. Seiffert^{TM} X-ray diffraction apparatus (XRD) was used at 4° grazing incidence with$Cu_{k\alpha}$ radiation to identify the nature of the oxides present in the oxide scales.

EXPERIMENTAL RESULTS

As-coated Microstructures

RT22/CMSX-4

Figure 1 shows the topography, morphology and microstructure of the surface of a RT22/CMSX-4 specimen in the as-coated condition. The secondary-electron image (Fig. 1a) shows the surface topography and reveals its heterogeneity with large protrusions and valleys with a granular structure. This surface topography is expressed through the parameter R_a reported in Table II. A back-scattered electron (BSE) image (Fig. lb) reveals the chemical composition heterogeneity. Protrusions are a mixture of two phases, β-NiAl appearing as a grey phase and $PtAl_2$ as a bright one. Black zones are covered by alumina grown during heat treatments under vacuum. The granular structure of valleys is confirmed by BSE image. Valleys are also composed of $PtAl_2$ and β-NiAl but a brighter phase located between β-NiAl grains can also be detected. This phase is neither $PtAl_2$ nor an oxide. It is rich in Ti and Ta as observed on an EDS elementary map (Fig. 2). Its chemical composition, as given by SEM-EDS analysis, is reported in Table III. As the analyzed areas are smaller than 1 μm, the reported values do not provide the actual chemical composition of this (Ti, Ta)-rich phase, Ti and Ta contents are certainly underestimated. According to the Ni–Ti–Al and Ni–Ta phase diagrams, respectively studied by Huneau *et al.*[27] and Ansara *et al.*,[28] this

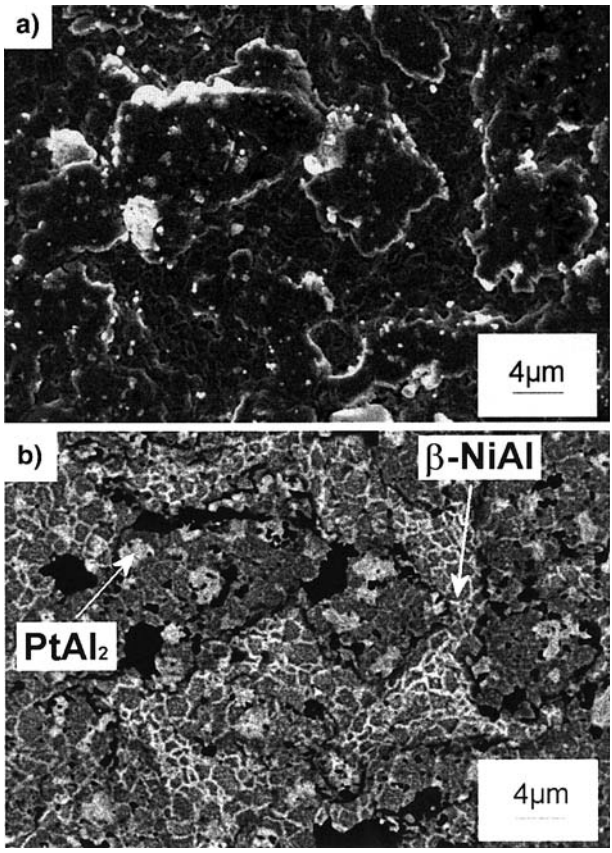

Fig. 1. The surface of RT22/CMSX-4: (a) secondary electron and (b) back-scattered electron images.

(Ti, Ta)-rich phase observed at the surface of RT22/CMSX-4 system is likely a solid solution Ni(Ti, Al, Ta)$_2$ of isostructural($Fd\bar{3}m$) $NiTi_2$, $NiAl_2$ and $NiTa_2$ intermetallic compounds. This phase is too thin to be clearly identified in SEM of cross sections. Nevertheless, an EDS map of the chemical elements[26] on a cross-section, revealed a thin phase enriched in Ti and Ta and without O close to the coating surface.

Cross sections of RT22 coating on CMSX-4 show that it is a two-phase coating composed of several layers (Fig. 3a). Table III reports the chemical composition, measured by TEM–EDS and SEM–EDS, of the phases and precipitates observed in as-processed RT22/CMSX-4 system. Data reported are concentration ranges resulting from several measurements obtained on several zones and precipitates. Large fluctuations are either due to

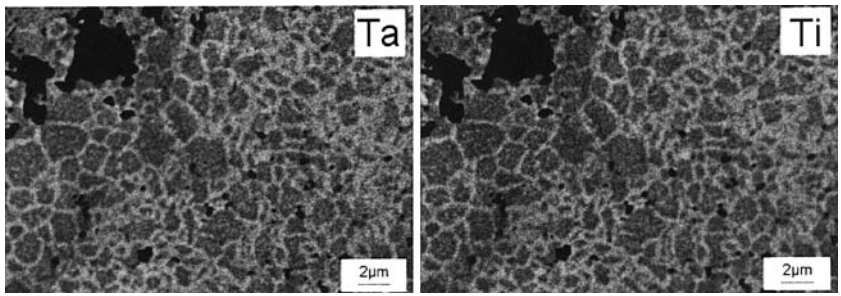

Fig. 2. EDS maps of Ti and Ta performed at the surface of RT22/CMSX-4 before oxidation showing Ti and Ta-rich phase between β-NiAl grains.

Table III. Chemical Composition (at.%) Measured by TEM–EDS and SEM–EDS of Phases and Precipitates Encountered in RT22/CMX-4 before oxidation

Phase	Method	Al	Ti	Cr	Co	Ni	Mo	Ta	W	Pt	Re
β-NiAl	SEM–EDS	**49–51**	0	1	4	34–36	1	0	0–1	**7–8**	1
(zone 1,2)	TEM–EDS	**38–47**	2–5	0.5–4	3–5	26–43	0	0–2	0–1	**6–21**	0
β-NiAl	SEM–EDS	**38–47**	0–1	1–4	5–7	40–50	0	0–1	0–1	0–3	0–1
(zone 3,4,5)	TEM–EDS	**32–47**	1–3	1–4	5–8	42–54	0	0–1	0–1	0–5	0–1
$PtAl_2$	SEM–EDS	**54–55**	0–1	4–7	2–3	13–17	1	0	0	**20–21**	0
(zone 1,2)	TEM–EDS	**44–46**	5–6	6–7	2	9–10	0	0–2	0	**31**	0
α-w (zone 1,2,3)	TEM–EDS	2–10	6–11	1–5	1–2	6–15	2–5	**24–35**	**32–40**	0–7	**8–10**
σ (zone 3)	TEM–EDS	1–2	5–7	**34–35**	2–5	6–10	1–8	**20–26**	**6–8**	1–2	**13–16**
μ (zONE 4,5)	TEM–EDS	0–4	3–5	**18–32**	**12–14**	13–22	1–5	**8–19**	**11–21**	0	**7–12**
α-Cr (zone 5)	TEM–EDS	1–2	2-3	**48–49**	**18–19**	10–11	1–2	4–5	6–7	0	**5–6**
γ'-Ni_3Al	SEM–EDS	**20**	2	4	9	60	0–1	4	0	0	0
(zone 4,5,6)	TEM–EDS	**9–18**	2–5	0–3	6–9	62–68	0–1	3–6	0–3	0–1	0
γ-Ni	TEM–EDS	2–3	1–2	**18–19**	18–19	47–48	1–2	1–2	3–4	0	3–4
Ti, Ta-rich phase btw β-NiAl grains	SEM–EDS (approxim)	< 28	> **23**	2	3	< 25	0–1	> **12**	1	< 4	1

occasional contribution from the matrix for small particles or actual local variations in composition. From the surface to the substrate, the following zones of differing contrast can be identified (Fig. 3a):

- A bright, 20 μm-thick, external zone (EZ), consisting in a mixture of β-NiAl and $PtAl_2$ phases. Two layers of differing composition and microstructure can be distinguished: (1) the external layer of columnar microstructure in which $PtAl_2$ is the predominant phase; (2) the internal and thicker layer characterized by an equiaxed microstructure and in which $PtAl_2$ and β-NiAl are homogeneously distributed.

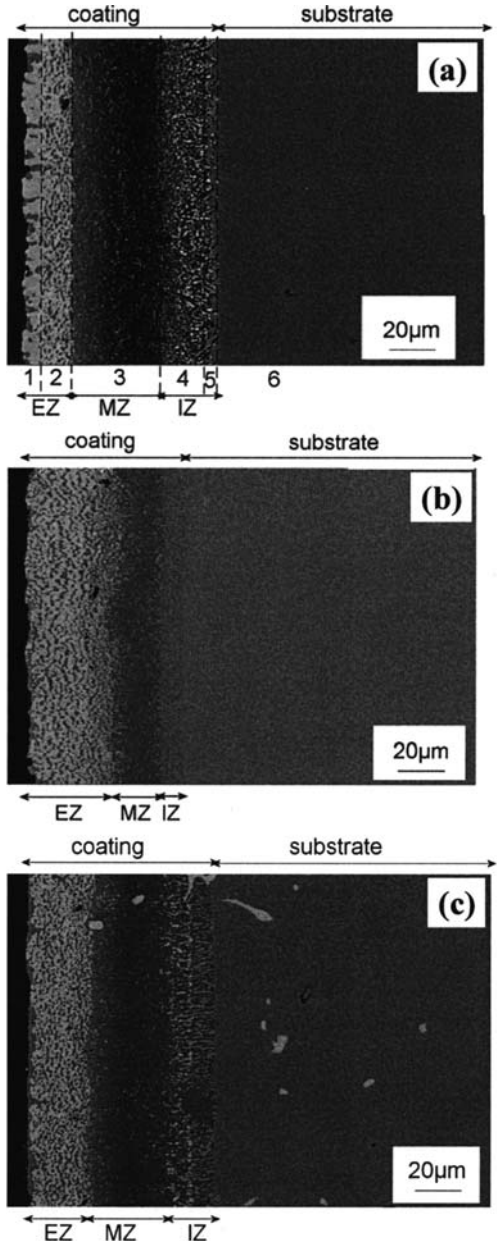

Fig. 3. Cross-section (SEM-BSE) of as-coated (a) RT22/CMSX-4 (b) RT22/SCB (c) RT22/IN792.

- A dark middle zone (MZ, layer 3), 45 μm thick, which consists on a single phase β-NiAl with numerous precipitates of α-W and σ-phase according to the work of Zhang *et at*.[29] and Angenete *et. al.*[2,3]
- An interdiffusion zone (IZ) 25 μm thick with a β-NiAl matrix containing γ' precipitates and precipitates rich in heavy elements.

These SEM observations were complimented by the TEM investigations shown in Fig. 4. In layer (2) of the EZ, in addition to β-NiAl and $PtAl_2$, round W-rich precipitates were observed. According to their chemical composition and to the literature,[2,3] they are identified as α-W particles. In layer (3), α-W and σ-phase precipitates are identified. In IZ, two layers can be distinguished: the layer (4) where precipitates are larger, round or blocky, they correspond to the rhombohedral μ-phase, and the layer (5) at the IZ/substrate interface, where Cr-rich precipitates were observed between coalesced

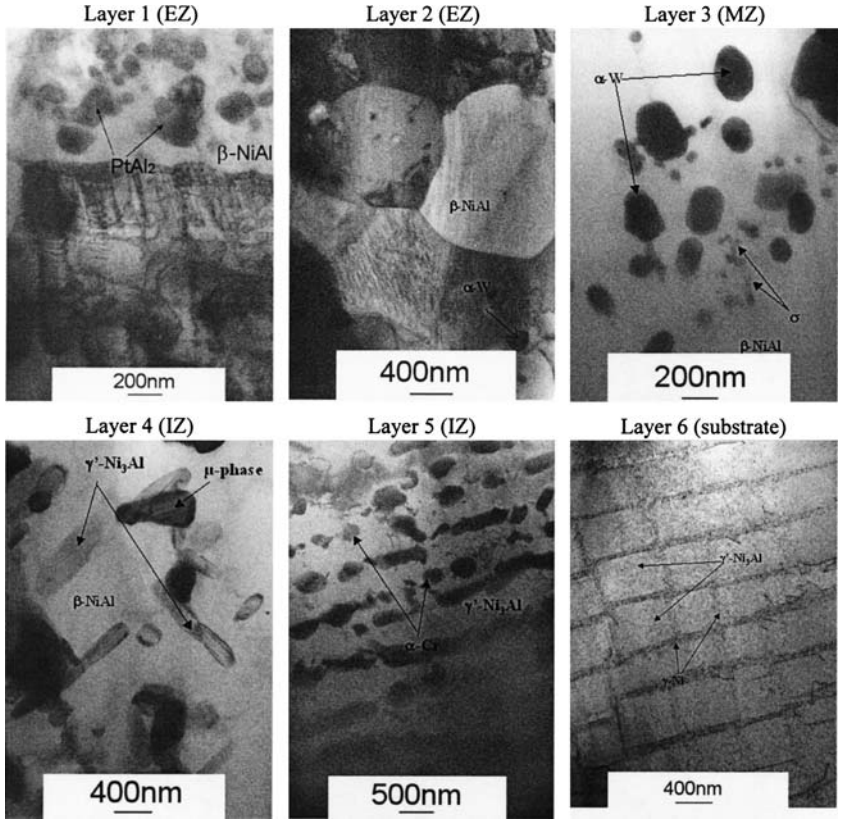

Fig. 4. TEM images of as coated RT22/CMSX-4 in several zones (layers refer to Fig. 3a).

γ' grains (rafting zone). These last precipitates, smaller than the μ-phase precipitates, are probably based on the bcc α-Cr phase. Finally the substrate (layer 6) has a typical microstructure of single-crystal superalloy with cuboïdal γ' precipitates in a γ phase matrix. In single-crystal superalloys, the precipitates γ' size remains within the range from 0.2 to 5 μm and their volume fraction can reach 70% at room temperature.[30] The characteristics of the superalloy studied are within these specifications.

RT22/SCB and RT22/IN792

The morphology and microstructure of as-coated RT22/SCB and RT22/IN792 specimens are shown in Figs. 5 and 6. Surface of RT22/SCB is

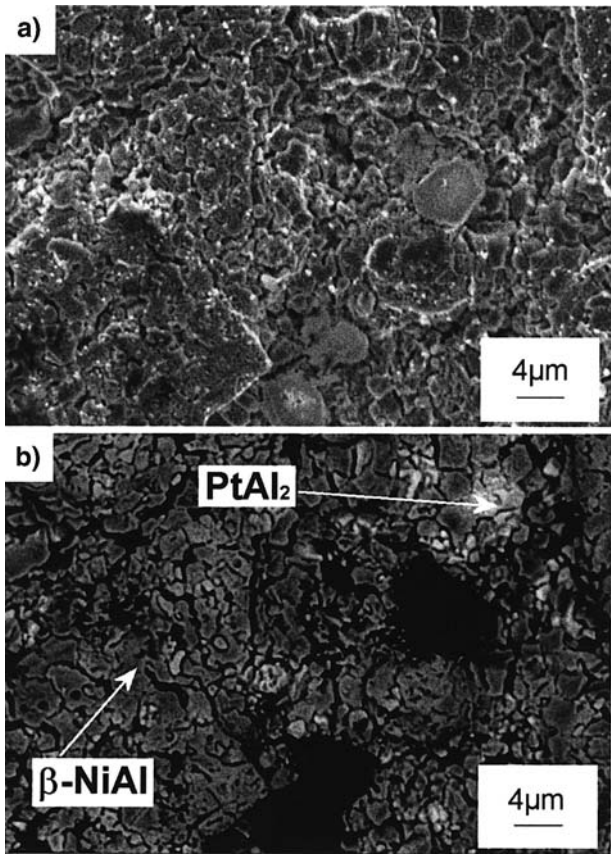

Fig. 5. The surface of RT22/SCB: (a) secondary electron and (b) back-scattered electron images.

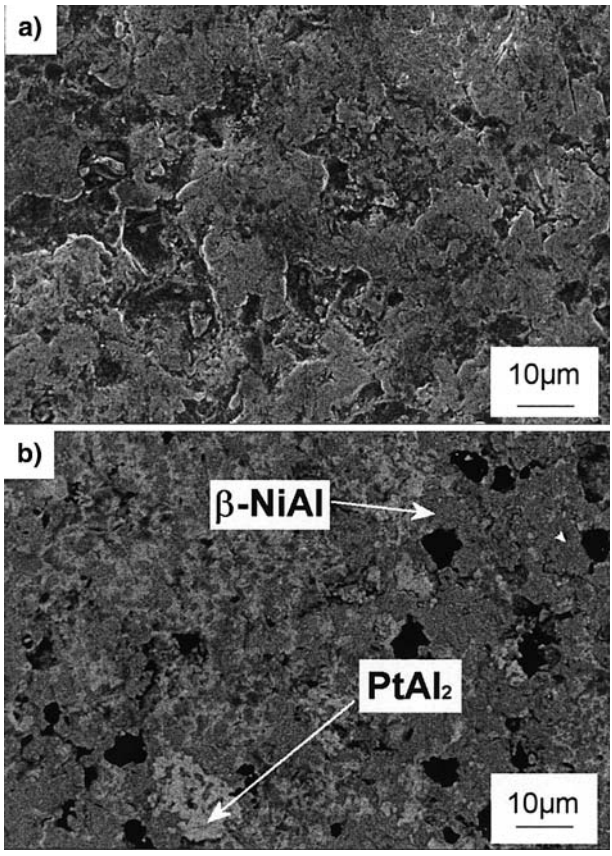

Fig. 6. The surface of RT22/IN792: (a) secondary electron and (b) back-scattered electron images.

also irregular and rough (Table II). Secondary-electron imaging (Fig. 5a) and BSE imaging (Fig. 5b) reveal a two-phase microstructure (β-NiAl and $PtAl_2$) with pores and Al_2O_3 grains. There are numerous pores but no protrusion on RT22/IN792 (Fig. 6a). Thus, the surface of this system appears smoother despite a similar R_a than the other systems (Table II). Back-scattered electron image of RT22/IN792 (Fig. 6b) confirms the two-phase microstructure (β-NiAl and $PtAl_2$) with Al_2O_3 grains grown during heat treatment. The Ti and Ta-rich phase, Ni(Ti, Al, Ta)$_2$, detected on RT22/CMSX-4 specimens was not observed on these coated specimens. This observation should be linked to the composition of the substrates but also to the effect of the heat treatments which are different for the three

systems. Then, Ti and Ta average concentrations were measured in the three systems after their heat treatment. RT22 on CMSX4 contains 1 at.% of Ta and 0.6 at.% Ti in average, whereas RT22 on IN792 contains 0.8 at.% Ta and 2.2 at.% Ti and RT22 on SCB contains only 0.2 at.% Ta and 1.4 at.% Ti. From these results it appears that a critical Ta content is certainly necessary to the formation of the Ti–Ta-rich phase at the surface of the RT22 coating.

The microstructure of the coating RT22 on SCB and on IN792 observed in cross-sections are shown in Fig. 3b and c. These two systems are composed of the same zones than RT22/CMSX-4 (EZ, MZ and IZ), but their chemical composition (respectively, given in Tables IV and V), thickness and nature of precipitates depend on the nature of the substrate superalloy and associated heat treatments. Precipitates in EZ of RT22/SCB are bcc α-W particles. In IZ, three types of precipitates are observed: bcc α-Cr phase, (Ti, Ta)-rich precipitates and tetragonal σ-phase. In RT22/IN792, large (Ti, Ta)-rich precipitates were found in EZ, MZ, IZ and in the substrate. Two others types of precipitates were identified: (Cr, Ta, W, Mo)-rich phase (prec 2) in MZ and IZ and tetragonal σ-phase in IZ. Their chemical compositions are reported Table V.

Table IV. Chemical Composition (at.%) Measured by SEM–EDS of Phases Encountered in RT22/SCB before Oxidation

Phase	Al	Ti	Cr	Co	Ni	Mo	Ta	W	Pt
β-NiAl(EZ)	56	0–1	0–1	2	35	0–1	1	1	4
β-NiAl(MZ)	53	0–1	1	2	41	0–1	0–1	1	1
$PtAl_2$(EZ)	58–59	1	4	1	10–12	1	0–1	0	21–23

Table V. Chemical Composition (at.%) Measured by SEM–EDS of Phases and Precipitates Encountered in RT22/IN792 Before Oxidation

Phase	Al	Ti	Cr	Co	Ni	Mo	Ta	W	Pt
β-NiAl(EZ)	51	1	2	5	37	0–1	0	0	5
β-NiAl(MZ)	48	1	1	6	44	0–1	0	0	1
β-NiAl(IZ)	35	5	7	7	45	0	0	0	0
$PtAl_2$(EZ)	54	1	8	2	12	1	0	0–1	20
γ'-Ni_3Al(IZ)	15	9	2	6	64	0	3	0	0
Prec 1(TiTa)	1–5	46–50	1–2	1	6–8	3–4	33–34	3–4	0
Prec 2	1	10	31	2	7	16	16	16	0
Prec 3(σ)	2	1	50–52	13	18	6	1	6	0

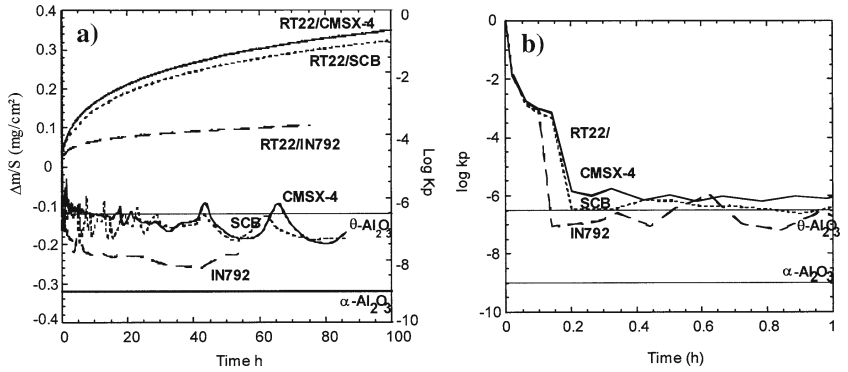

Fig. 7. (a) Mass-gain curves and k_p evolution at 900°C of RT22/CMSX-4, RT22/SCB and RT22/IN792. (b) enlargement of k_p evolution during transient stage.

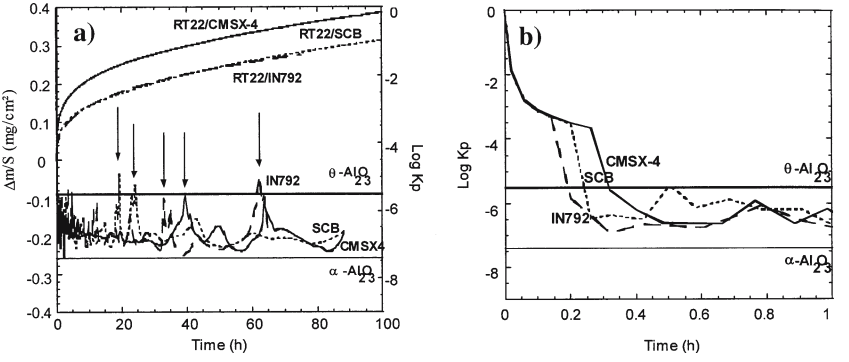

Fig. 8. (a) Mass-gain curves and k_p evolution at 1050°C of RT22/CMSX-4, RT22/SCB and RT22/IN792. (b) Enlargement of k_p evolution during transient stage.

Isothermal Oxidation Kinetics

Thermogravimetry data at 900, 1050 and 1150°C for RT22/CMSX4, RT22/SCB and RT22/IN792 systems are shown in Figs. 7a, 8a and 9a (continuous line), respectively. The first part of the curves is marked by fast and large mass gains and correspond to the transient stage during which all the stable oxides can form in addition to transient alumina. The second parts of the curves are parabolic. These mass-gain curves were analyzed using local fitting to a general parabolic law,[25] and the evolution of the parabolic rate k_p as a function of time is reported as dashed line in Figs. 7a, 8a and 9a. Enlargements of the transient stage are shown in Figs. 7b, 8b and 9b. Growth kinetics of α and θ-alumina, calculated according to literature data for a

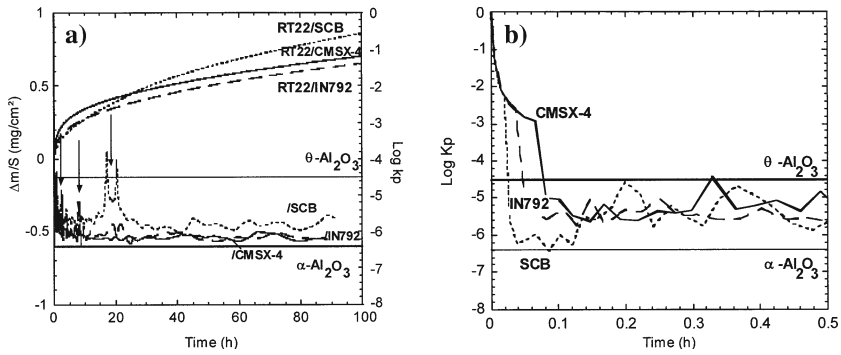

Fig. 9. (a) Mass-gain curves and k_p evolution at 1150°C of RT22/CMSX-4, RT22/SCB and RT22/IN792. (b) Enlargement of k_p evolution during the transient stage.

single-crystal NiAl[31] are additionally reported on the k_p curves. For the three coating systems, at 900, 1050 and 1150°C, the oxidation kinetics are parabolic, and the parabolic rate constant k_p varied slightly with time. Arrows mark several inflection points on mass change leading to a k_p "peak", for example at about 20 h at 1050°C for RT22/SCB. These inflection points of mass gain curves are probably due to oxide-scale cracking without spalling and subsequent healing, because k_p has about the same value before and after the "peak".

At 900°C (Fig. 7), the oxidation kinetics of RT22/CMSX-4 and RT22/SCB are quite similar with a high value of k_p and a steady-state stage which is not reached. After 100 h at 900°C, the oxidation kinetics are not yet fully controlled by α-alumina growth. On the contrary, RT22/IN792 has a parabolic rate constant k_p which is closer to the values corresponding to α-alumina growth on pure NiAl. At 1050 and 1150°C, a steady-state stage is reached for all coating systems, and the oxidation kinetics are controlled by α-alumina growth. But RT22/CMSX-4 has a slightly longer transient stage than RT22/SCB and RT22/IN792. This could indicate that transformation of transient alumina to a alumina is slower on RT22/CMSX-4 or that the nature of transient oxides grown on this system is different.

Cyclic Oxidation Kinetics at 900°C

Net mass changes per surface area (NMC) are reported, for each specimen, in Fig. 10. No mass loss was detected even after 52 cycles of 300 h (i.e.,15,600 h). That means there was no spallation or rather that the amount of oxide spalled during cooling was systematically lower than the

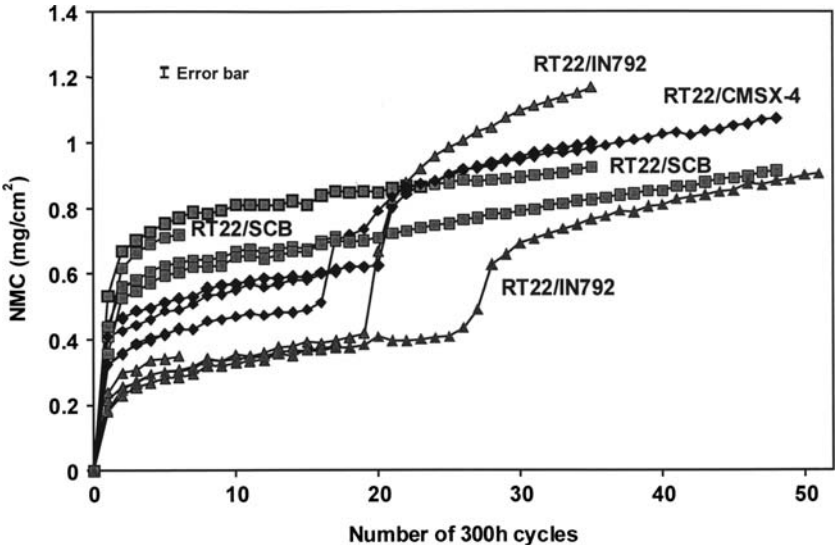

Fig. 10. Net mass change at 900°C of each coating system after 6 cycles, 17 cycles, 35 cycles and 52 cycles 300 h (i.e., 1800, 5100, 10,500 and 15,600 h).

amount of oxide grown during high-temperature dwell. Figure 10 shows clearly that for all samples (three of each system), RT22/SCB system has a faster oxidation rate than RT22/CMSX-4 and than RT22/IN792, at least during the first 16 cycles (i.e., 4800 h). The higher kinetics for the SCB substrate may be due to the lack of Hf and Zr in this alloy, as reactive elements are known to reduce the growth kinetics of α-Al_2O_3. This explanation would be also consistent with the lowest oxidation kinetics after 16 cycles, observed with the IN792 substrate which has the highest Hf level. If this is the case, Hf and Zr are in small quantity in the oxide since no RE was detected with EDS in the SEM and TEM.

After respectively 16 (or 20) cycles and 26 cycles of 300 h (marked by arrows), the oxidation kinetics increased suddenly for RT22/CMSX-4 and RT22/IN792. These fast mass changes can be attributed to the cracking of the alumina scale permitting a faster inward-oxygen diffusion with limited scale spallation. Indeed, assuming that there was only negligible spalling, the local fitting of the general parabolic law was used on the cyclic mass-change curves. It is then possible to calculate the parabolic rate constants before and after the sudden change of slope. The k_p obtained with cyclic-oxidation curves are compared in Table VI with k_p calculated from TGA curves and with literature data. As expected, after longer oxidation duration, k_p is

Table VI. Comparison of parabolic rate constants k_p($mg^2\ cm^{-4}\ s^{-1}$) calculated according to isothermal and cyclic mass change curves at 900°C, and values from the literature

	RT22/CMSX-4	RT22/SCB	RT22/IN792
k_p isothermal at 100 h	5.8×10^{-8}	9.5×10^{-8}	9.3×10^{-9}
k_p cyclic before mass jump	2.9×10^{-9}	5.2×10^{-9}	$1.6. \times 10^{-9}$
k_p cyclic after mass jump	3.5×10^{-9}		$5.0. \times 10^{-9}$
k_p isothermal for θ-Al_2O_3		2×10^{-7}	
k_p isothermal for α-Al_2O_3[a]	8×10^{-10}		

[a] This value is extrapolated from 1400 to 950°C data obtained on pure NiAl by Burmm and Grabke[31].

closer to the value corresponding to α-alumina growth. The k_p calculated after the sudden mass raise (i.e., after probable cracking) is similar to the k_p calculated before the jump which indicates that the resulting fast oxygen diffusion permits the rapid healing of the protective α-Al_2O_3 scale.

XRD Investigations

Comparison of the three coating systems diffractograms (Figs. 11–13) reveals some differences between the three systems RT22/CMSX-4, RT22/SCB and RT22/IN792. In the following description, distinction is made between metallic and oxide-scale phases.

Metallic Phases

Before oxidation, XRD confirms that RT22 is a two-phase coating consisting in a mixture of $PtAl_2$ and β-(Ni, Pt)Al, on the three superalloys. According to the Ni–Pt–Al phase diagram proposed by Gleeson *et al.*,[32] $PtAl_2$ transforms into β-(Ni, Pt)Al by losing Al and by gaining Ni when its Pt content is constant. In the present study, $PtAl_2$ is still detected in the three systems after 100 h isothermal oxidation at 900°C. This means that the amount of Al lost by oxidation and diffusion and the amount of Ni gained by diffusion after this treatment is not sufficient to transform all the $PtAl_2$ phase into β-NiAl, whereas the same duration at 1050°C or 1150°C is sufficient. After a large Al consumption by oxidation and interdiffusion, β-NiAl transforms fully to γ'-Ni_3Al. This was shown by XRD and SEM for the three coated superalloy systems after 100 h at 1150°C (Fig. 17 g–i). However, 35 cycles of 300 h at 900°C were not sufficient to transform all the β-NiAl to γ'-Ni_3Al.

Oxide Scales

All systems formed α-Al_2O_3 on the surface, but some significant differences were revealed by XRD. The first one concerns the nature of the

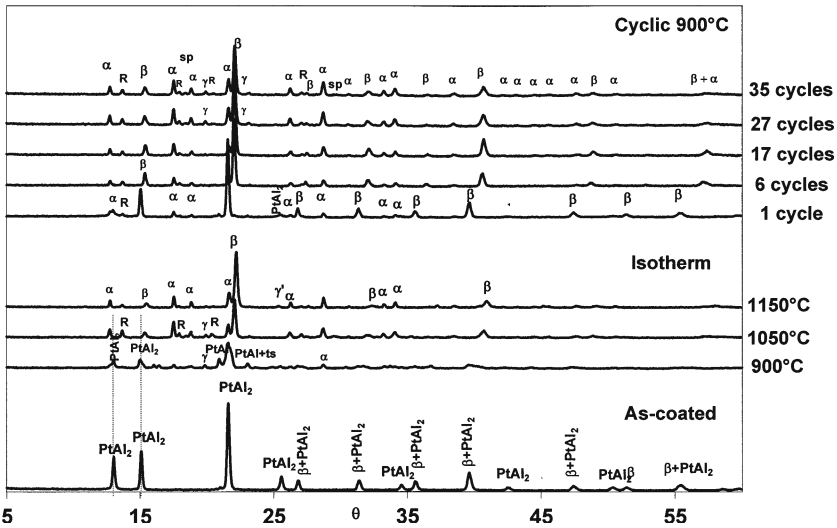

Fig. 11. XRD diagrams for RT22/CMSX-4. β stands for β-NiAl, γ' for γ'-Ni_3Al, α for α-Al_2O_3, γ for γ-Al_2O_3, R for rutile oxide TiO_2 or mixed (Ti, Ta)$_2O_4$, sp for spinel $NiAl_2O_4$ or others.

transient oxide detected. Indeed, RT22/CMSX-4 and RT22/IN792 formed the transient alumina γ-Al_2O_3 (Figs.11 and 13) whereas RT22/SCB formed θ-Al_2O_3 (Fig. 12). The second point is that after 100 h isothermal oxidation at 900°C these transient oxides were detected only on RT22/CMSX-4 (i.e., γ-Al_2O_3) and RT22/SCB (i.e.,θ-Al_2O_3). This is in good agreement with the parabolic rate constants k_p previously calculated (Fig. 7) which show that oxidation kinetics at 900°C are controlled by α-Al_2O_3 growth only for RT22/IN792.

During a long-term, cyclic-oxidation test at 900°C, peaks of transient alumina θ-Al_2O_3 on RT22/SCB (Fig. 12) disappeared with increasing number of cycles because of the θ-to-α-Al_2O_3 transformation. But peaks of γ-Al_2O_3 on RT22/CMSX-4 (Fig. 11) and RT22/IN792 (Fig. 13) first disappeared and then reappeared after extended cyclic oxidation (27 and 35 cycles for RT22/CMSX-4 and 21 cycles for RT22/IN792). This observation will be discussed later. The final point concerns the rutile oxide TiO_2 (or a mixed rutile oxide) which is detected only on RT22/CMSX-4 and RT22/IN792 (Figs. 11 and 13), i.e., transient alumina γ-Al_2O_3 is detected when rutile oxide is also detected. A possible correlation between rutile oxide and γ-Al_2O_3 formation will be discussed in the following.

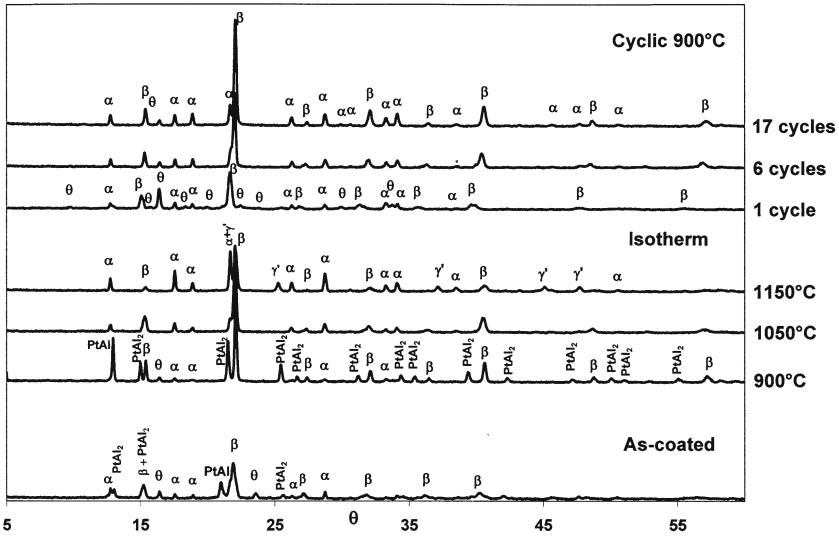

Fig. 12. XRD diagrams from RT22/SCB. β stands for β-NiAl, γ' for γ'-Ni_3Al, α for α-Al_2O_3, θ for θ-Al_2O_3.

Microstructural Investigations

Oxide Scale Surface Morphologies After 100 h at 900°C

Surfaces of all specimen were examined using SEM after 100 h at 900°C. Morphologies of the oxide scales formed at this temperature are shown in Fig. 14. At 900°C, whiskers were observed on all coating systems. This is a typical transient-alumina morphology that indicates cationic growth.[33] Whiskers are less numerous on RT22/IN792, which is consistent with XRD diagrams (Fig. 13) where transient oxide is not detected on RT22/IN792 after 100 h at 900°C and with thermogravimetry results (Fig. 7) which show that the oxidation kinetics are controlled by α-Al_2O_3 growth only on RT22/IN792.

Oxide Scale Surface Morphologies After 100 h at 1050°C

After 100 h at 1050°C (Figs. 11–13), the scale is composed mainly of α-Al_2O_3 on the three systems except on RT22/CMSX-4 and RT22/IN792 which also contain transient alumina γ-Al_2O_3 and rutile oxide TiO_2 or mixed rutile oxide $(Ti, Ta)_2O_4$. In both cases, small whiskers were observed, and spalled zones were detected on RT22/CMSX-4 (Fig. 15a).

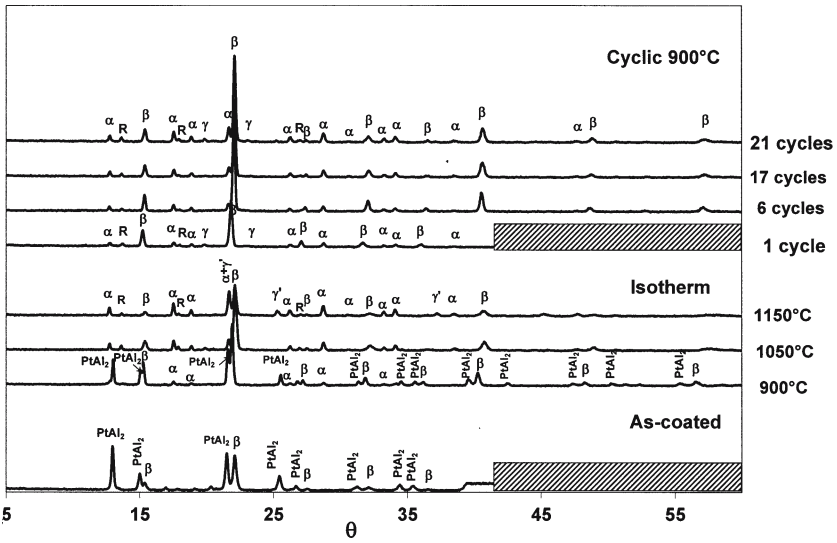

Fig. 13. XRD diagrams from RT22/IN792, β stands for β-NiAl, γ' for γ'-Ni_3Al, α for α-Al_2O_3, γ for γ-Al_2O_3, R for rutile oxide TiO_2 or mixed, sp for spinel $NiAl_2O_4$ or others.

Oxide-Scale-Surface Morphologies After 100 h at 1150°C

Surface morphologies observed at this temperature are reported on Fig. 16. The oxide scale consists mainly of α-Al_2O_3 on the three systems, and the oxide scale is dense without whiskers, When rutile oxide or mixed rutile oxide were identified by XRD, as for RT22/CMSX4 and RT22/IN792 systems (Figs. 11 and 13), large spalled zones and cracks were observed in the oxide scales (Fig. 16c).

Oxide Scale Cross-sectional Morphologies

Cross-sectional morphologies of oxide scales observed by SEM are reported on Fig. 17. Oxide-scale thickness was determined from several measurements (about 10) on several SEM images corresponding to different zones on the cross-section (random choice). Undulations were observed at the metal/oxide interface of RT22/CMSX-4 at 900°C (a) and 1050°C (Fig. 17d). That leads to a variable thickness (between 2.4 and 4.4 μm). These undulations are not connected to the initial roughness, as it is the case for RT22/SCB at 1150°C (Fig. 17 h). Indeed, for RT22/CMSX4 (Fig. 17a, d) metal/oxide and oxide/gas interfaces do not follow the same undulation.

For RT22/SCB and RT22/IN792 oxidized at 1050°C, the measured average oxide-scale thickness is well correlated to the mass gain during the

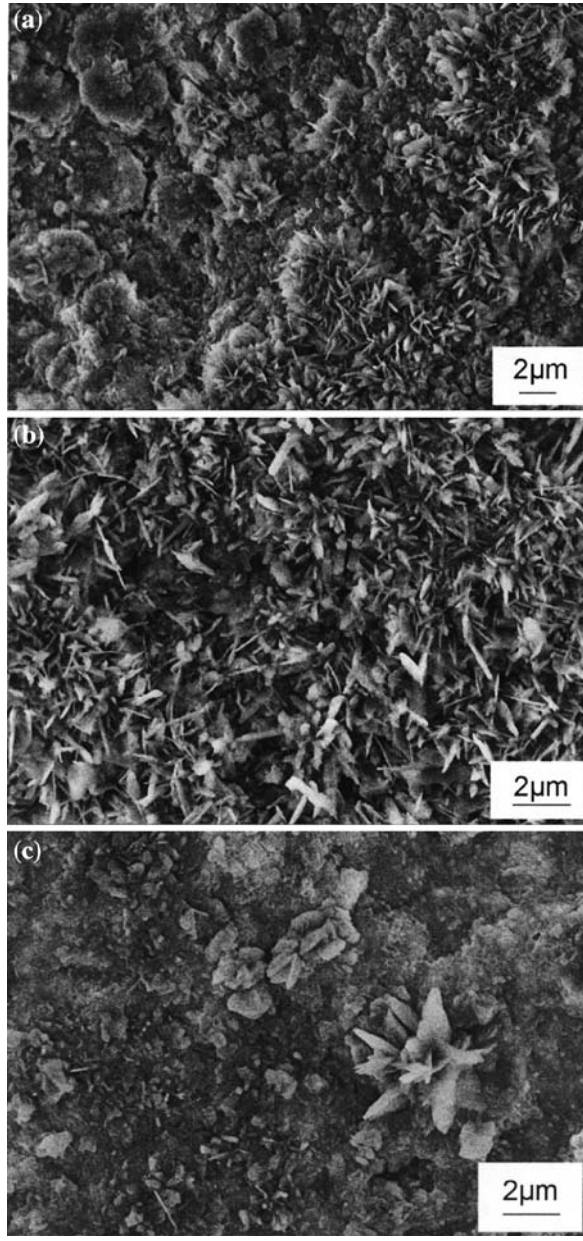

Fig. 14. Oxide-scale surface after 100 h at 900°C in synthetic air of (a) RT22/CMSX-4 (b) RT22/SCB, (c) RT22/IN792.

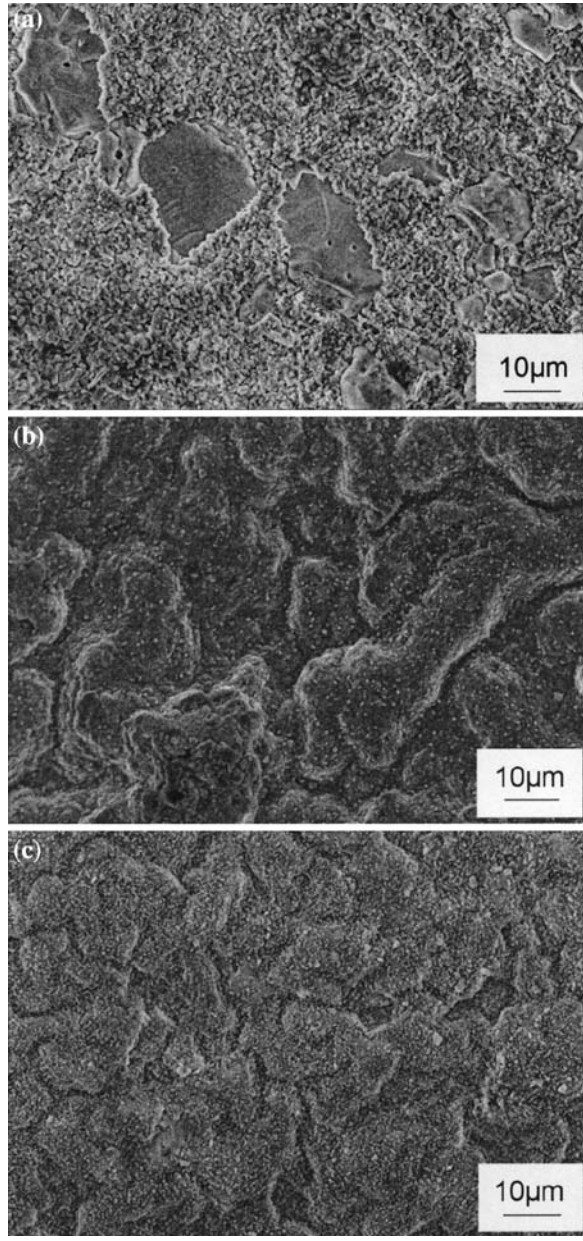

Fig. 15. Oxide-scale surface after 100 h at 1050°C in synthetic air on (a) RT22/CMSX-4 Large smooth area are spalled zones, (b) RT22/SCB, (c) RT22/IN792.

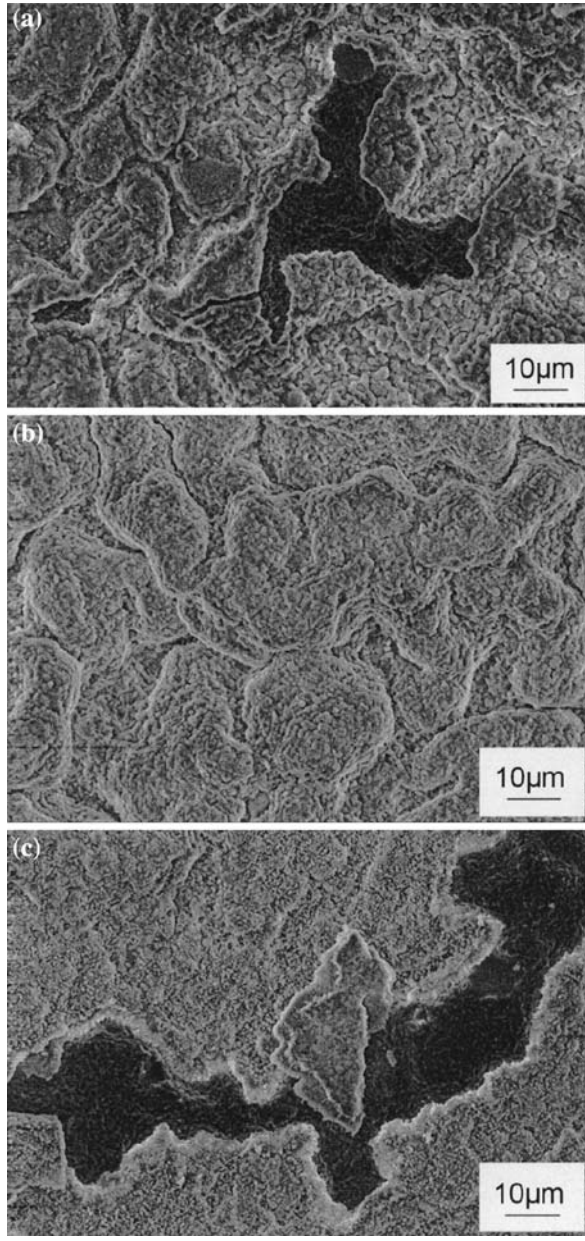

Fig. 16. Oxide-scale surface after 100 h at 1150°C in synthetic air on (a) RT22/CMSX-4, (b)RT22/SCB, (c) RT22/IN792.

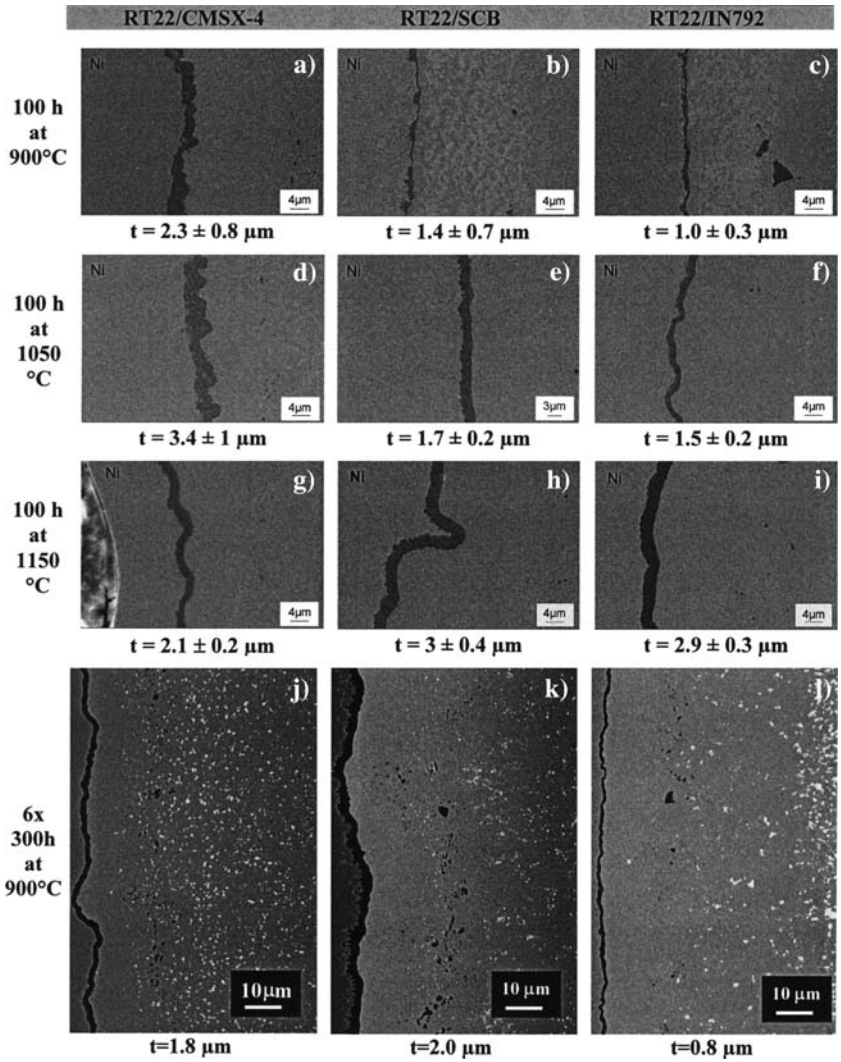

Fig. 17. Cross-sections of oxide scale observed by SEM (secondary electron) on the three coating systems after isothermal oxidation at 900°C (a, b, c), 1050°C (d, e, f) and 1150°C (g, h, i), in synthetic air, after cyclic oxidation at 900°C (j, k, l) in laboratory air.

high-temperature dwell of the TG analysis, assuming α-alumina formation (0.185 mg/cm^2 for a 1 μm scale). This is not the case for the RT22/CMSX4 system at 1050°C nor for the three systems at 900°C, for which the actual

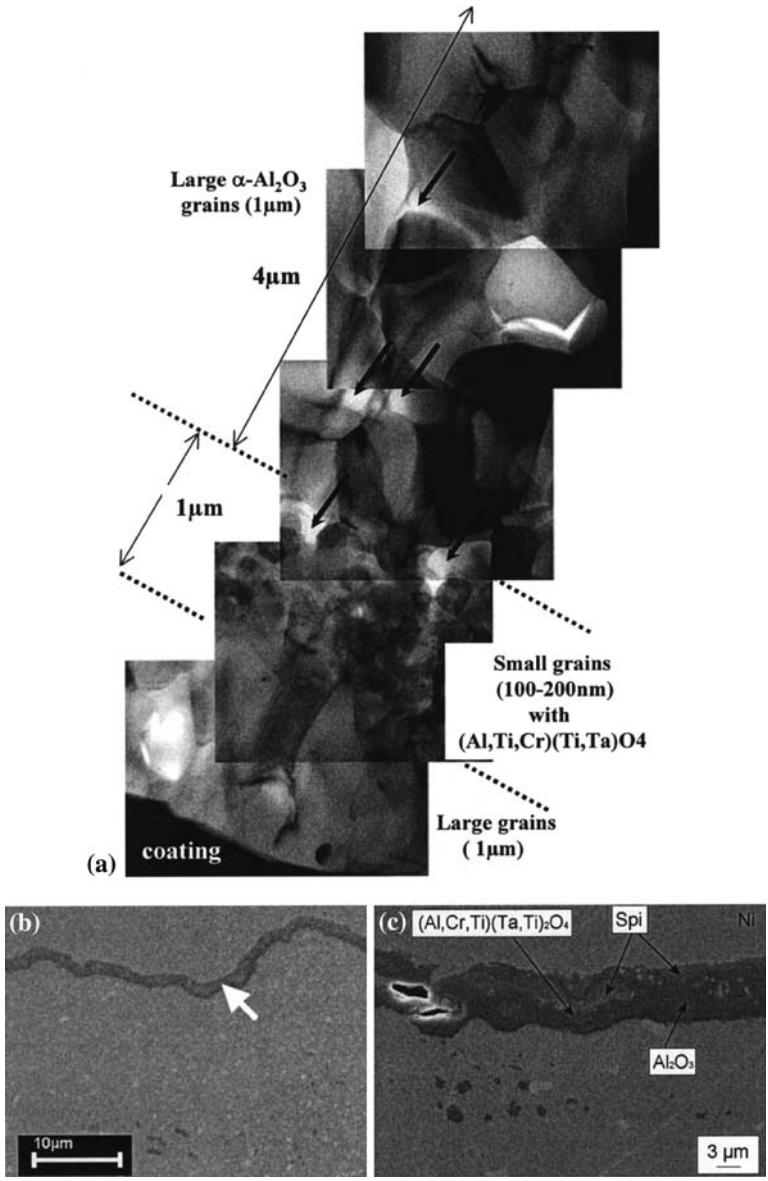

Fig. 18. (a) TEM cross-section of the oxide formed on RT22/CMSX-4 after 100 h at 1050°C in synthetic air. (b) Localization (white arrow) of the (Al,Ti,Cr)(Ti,-Ta)O_4 midle layer in the oxide scale formed on RT22/CMSX-4 after six cycles of 30 h at 900°C (SEM-SE) (c) after 6×300 at 1050°C.

oxide-scale thickness is larger of 25–40% than expected from the mass gain at high temperature. This difference can be attributed to the amount of oxide formed during heating in the TGA (the mass gain during heating is not reported in Figs.7–9).

It can be seen also on Fig. 17j–l the oxide-scale thickness after cyclic oxidation at 900°C is well correlated with mass gains shown on Fig. 10, with a thicker oxide scale for the RT22/SCB system and a thinner oxide scale for the RT22/IN792 system.

Oxide scale formed on RT22/CMSX-4 after 100 h at 1050°C was also analyzed by TEM with EDS (Fig. 18a). This examination reveals that three zones could be distinguished : (1) an internal zone (1 μm thick) close to the metal/oxide interface, formed of large α-Al_2O_3 grains, (2) a middle zone (1 μm thick) with small grains, analyzed to be a Ti, Ta-rich oxide, (3) an external zone (4 μm thick) composed of large α-Al_2O_3 grains and where cavities can be observed (marked with arrows). The Ti, Ta-rich oxide probably corresponds to the rutile oxide detected by XRD. Its chemical composition was measured by EDS (Table VII). Note that the quantification of O by EDS is difficult so the chemical composition reduced to metallic elements was also reported in Table VII. Ti, Ta-rich rutile oxides which can be formed on RT22/CMSX-4 are TiO_2 $AlTaO_4$, $CrTaO_4$, $NiTA_2O_6$, $CoTa_2O_6$ or $CrTa_2O_6$. Lattice parameters of these oxide phases are close to each other, so it was difficult to distinguish them by XRD or by electron diffraction in the TEM. Mixed oxides can also form. The ternary phase diagram $AlTaO_4$–$CrTaO_4$–TiO_2 has been studied at 1200°C.[34] It was found that a continued solubility of $CrTaO_4$ and TiO_2 exists at this temperature. That means that the rutile oxide observed on RT22/CMSX-4 is probably a solid solution (Al,Cr,Ti)(Ta,-Ti)O_4 where Al^{3+}, Cr^{3+} and Ta^{5+} are randomly distributed on cationic sites.

This middle layer of Ti–Ta rich oxide was also observed by TEM on RT22/CMSX-4 samples after 6 and 17 cycles of 300 h oxidation at 1050°C[26] and by SEM after 6 × 300 h cyclic oxidation at 900°C (Fig. 18b) and 1050°C (Fig. 18c).

Table VII. TEM–EDS analyse of the Ti, Ta-rich oxide formed on RT22/CMSX-4 after 100 h at 1050°C

%at.	AI	Ti	Cr	Co	Ni	Mo	Ta	W	Pt	O
Rutile	11–14	40–46	0–1	0–1	1–2	0	2–4	0	0	34
Oxide	18–21	64–69	0–1.5	0–1.5	1.6–3	0	3–6	0	0	

DISCUSSION

The microstructure, composition and morphology of as-coated systems are complex and influenced by the nature of the substrate as it was highlighted by SEM and TEM investigations. According to the literature,[29,35] the coating system RT22/CMSX-4 which is commonly used in service, is usually a single-phase coating with an external part which consists of β-NiAl rich in Pt. But the RT22/CMSX-4 coating, although prepared under industrial conditions, is a two-phase coating. This two-phase microstructure was also observed by Göbel *et al.*[4] on RT22 deposited on two other single-crystal superalloys CMSX-6 and SRR 99. The coating microstructure depends on the thickness of the initial platinum deposit,[36,37] on diffusion heat treatments after Pt deposition and on the parameters of aluminization (Al content, duration).[38]

Although the three systems are two-phase coatings prepared under the same conditions, the surface morphologies, compositions and microstructures observed on cross sections are different. The roughness is quite similar on the three systems but the observed topographies revealed some differences and surface heterogeneities. The thickness of the different coating zones (EZ, MZ and IZ) depends also on the superalloy substrate. The main difference between the coating systems studied is the chemical composition at the surface. Particularly, the Ti and Ta-rich phase Ni(Ti, Al, Ta)$_2$ which was observed at the surface between β-NiAl grains on RT22/CMSX-4 (Figs, 1 and 2). All these differences are related to the composition of the substrate and the associated thermal treatments. They influence scale the growth kinetics, oxide-scale morphology, microstructure and composition.

Oxide-Scale Growth and Effect of Substrate Alloying elements (Ti and Ta)

During isothermal oxidation, it was shown that the transient-oxidation stage was slightly longer for RT22/CMSX-4. According to this observation and to XRD and microstructural investigations, it can be proposed that during this transient-oxidation stage, transient alumina first forms on β-NiAl, $PtAl_2$ and Ni(Ti, Al, Ta)$_2$. Because of the fast growth of transient alumina, the Ni(Ti, Al, Ta)$_2$ phase becomes Al-depleted and forms Ti,Ta-rich oxides of the rutile-type such as the mixed oxide (Al, Cr, Ti)(Ta, Ti)O_4 which was detected by XRD (Fig. 11) and observed on TEM cross sections (Fig. 18a). Then γ-Al_2O_3 transformed to α-Al_2O_3 leading to the steady-state stage controlled by α-Al_2O_3 growth. TEM cross sections on specimens oxidized for 100 h at 1050°C showed that the rutile oxide (Al, Cr, Ti) (Ta, Ti)O_4 layer rests between two large-grain alpha-alumina layers, the external

one being 4 μm thick and the internal one 1 μm thick. This observation suggests a cationic growth of the transient alumina followed by the growth of Ti, Ta-rich rutile oxide at the metal/oxide interface. Then the transient alumina transformed to stable α-alumina with the simultaneous internal α-alumina growth by anionic growth. This change of growth mechanism (i.e., cationic to anionic) and the volume change associated with the transformation of transient alumina to alpha alumina can explain the presence of cavities within the external part of the oxide scale (marked with arrows on Fig. 18a). Such a mechanism (Fig. 19a) can explain also the undulations observed at the metal/oxide interface of RT22/CMSX-4 which can not be attributed to the initial surface roughness.

XRD showed that rutile oxide also formed on RT22/IN792 at 1050 and 1150°C. As no TEM observation was done on this system, it cannot be concluded that this rutile oxide had the same location and origin as the rutile oxide grown on RT22/CMSX-4. Moreover, the Ni (Ti, Al, Ta)$_2$ phase leading to (Al, Cr, Ti)(Ta, Ti)O_4 formation was not observed on RT22/IN792, and the oxide-scale morphology was not the same, nor the transient oxidation stage which was not as long as on RT22/CMSX-4. As a consequence, it is thought that rutile oxide on RT22/IN792 did not form by the same mechanism as on RT22/CMSX-4. As shown in Fig. 19b and as already proposed by Göbel for RT22/CMSX-6,[4] rutile oxide probably grew

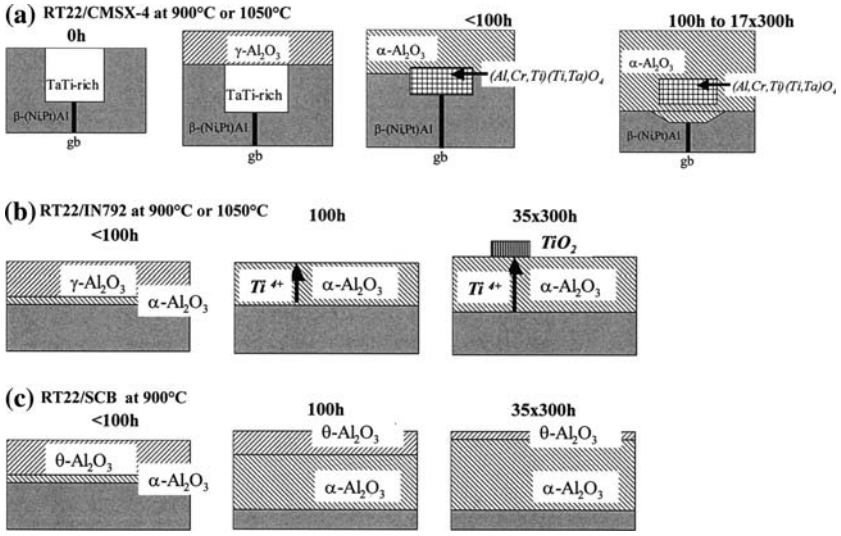

Fig. 19. Oxide-scale-growth mechanism during short isothermal oxidation at 900 or 1050°C in synthetic air of (a) RT22/CMSX-4, (b)RT22/IN792, (c)RT22/SCB.

on RT22/IN792 by fast-Ti diffusion from the substrate to the external-oxide surface where it can form TiO_2 above the existing alumina scale.

On RT22/SCB, no rutile oxide was detected after isothermal oxidation at 900°C and 1050°C. Transient oxide θ-Al_2O_3 was only partially transformed to α-Al_2O_3 after 100 h at 900°C but also after 35 cycles of 300 h at 900°C (Fig. 20), Whereas after 100 h at 1050°C, the oxide scale consisted exclusively of α-Al_2O_3. On this coating system, the oxide scale was dense, adherent, continuous and can grow according to the mechanism proposed in Fig. 19c. Cracks and spallation were observed only when rutile oxide is detected by XRD. This Ti, Ta-rich oxide which has grown on RT22/CMSX-4 and RT22/IN792 according to mechanisms proposed in Fig. 19 appears responsible for crack formation in the oxide scale and thus promotes spallation. The presence of Ti (and/or Ta) in oxide scale is often reported as detrimental to alumina-scale spallation resistance.[4,19–23] It is still unclear how Ti (and/or Ta) leads to cracking and promotes spallation. Some authors suggested that fast diffusion of Ti to the surface leads to TiO_2 formation above Al_2O_3 and enhances the oxide-scale growth rate.[4,20,21] Other authors[39] proposed that Ti promotes development of Ti-rich oxide protrusions at the metal/scale interface and that these protrusions introduce a complex stress state which initiates the formation of cracks.

Cracking and spallation result from stresses generated in the oxide scale. Two types of stresses exist in oxide scales: growth stresses which develop during the oxidation process and thermal stresses due to thermal-expansion-coefficients mismatch between the oxide scale and the metal. Thermal-expansion coefficients (CTE) of Al_2O_3 and TiO_2 are similar at 1050°C as $CTE(Al_2O_3) = 8.5 \times 10^{-6}K^{-1}$ $CTE(TiO_2O_3) = 8.4 \times 10^{-6}K^{-1}$.[40] Then, thermal stress are not enhanced by TiO_2 formation. The origin of growth stresses is more complex and not fully understood. However, it is commonly accepted that the growth stress is strongly affected by the relative molar volumes in the metal and in the oxide, the crystal structures of oxide and metal, and the growth mechanisms of the oxide.[14] When an oxide forms at the metal/oxide interface, the volume change due to the oxide formation can be expressed by the Pilling and Bedworth ratio (PBR).[41] PBR of Al_2O_3 and TiO_2 grown on NiAl alloy can be easily calculated from the corresponding molar volumes. It is found that $PBR(Al_2O_3/NiAl) = 1.8$ and $PBR(TiO_2/NiAl) = 2.6$. This huge difference means that TiO_2 growth on RT22/CMSX-4 should introduce large local compressive stresses in the oxide scale, which adds to the compressive thermal stress during cooling and may promote local cracking or spallation.

On the contrary, for the RT22/IN792 system, if Ti^{4+} cations diffuse through the oxide scale to form TiO_2 on top of Al_2O_3, this should not result in additional stress. On RT22/SCB, rutile oxide is not observed and the

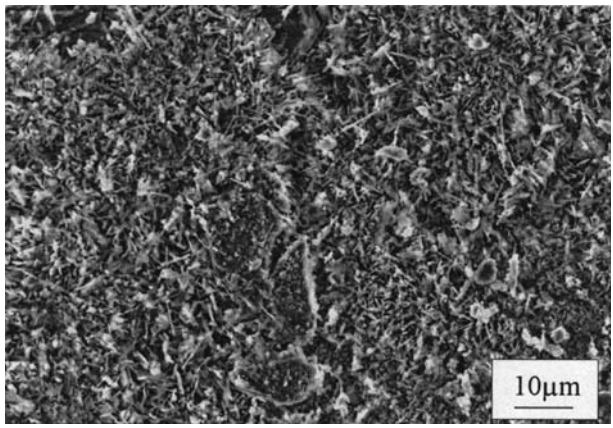

Fig. 20. SEM image showing transient alumina on surface of RT22/SCB after 35 cycles of 300 h at 900°C in laboratory air.

transformation of transient alumina (i.e.,θ-Al_2O_3 to α-Al_2O_3) seems delayed (Fig. 20) compared to RT22/CMSX-4 and RT22/IN792. Several authors also reported that the presence of Ti in the oxide scale, during oxidation of (Ni,Pd)Al coating[23] or β-NiAl alloy[13,42] tends to accelerate the transformation of θ-Al_2O_3 to α-Al_2O_3.

The present work shows that, in the RT22/CMSX-4 and RT22/IN792 systems, the formation of TiO_2, (or mixed rutile oxide) comes together with a faster γ-Al_2O_3 to α-Al_2O_3 transformation. A faster transformation is beneficial to the oxidation kinetics, but can be detrimental to the spalling behavior for two reasons. The first one is that this transformation corresponds to a molar volume reduction, then the associated strains cause tensile stress in the oxide scale during high-temperature dwells. This tensile stress generally induces some-oxide scale cracking. But for these short oxidation times, healing will occur at the cracks. The second reason is that the alumina transformation reduces the level of compressive growth stress which adds to thermal compressive stress to cause spalling during cooling. Then, a slow transformation may be beneficial by reducing spalling during

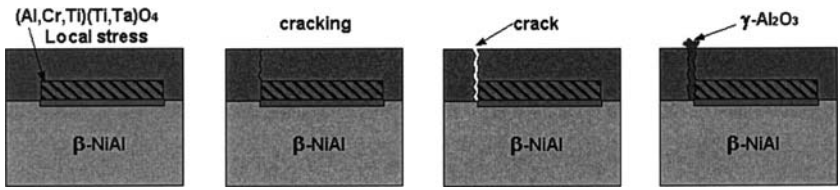

Fig. 21. Oxide-scale cracking on RT22/CMSX-4 during long-term cyclic oxidation at 900°C in laboratory air.

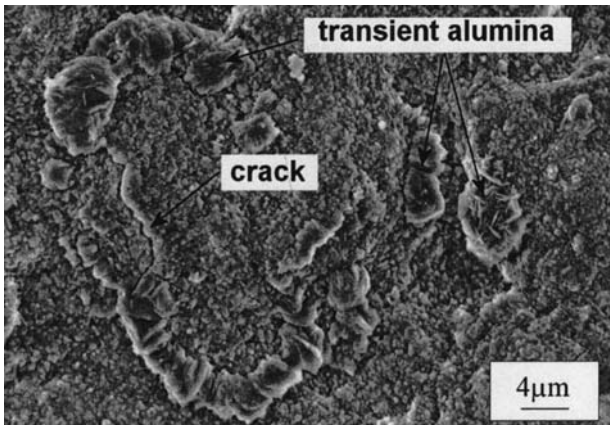

Fig. 22. SEM image showing transient-alumina growth close to cracks on the surface of RT22/IN792 after 35 cycles of 300 h at 900°C in laboratory air.

cooling during a larger number of cycles. Cracking of the oxide scale could explain the raise of RT22/CMSX-4 and RT22/IN792 mass gains during long-term cyclic oxidation at 900°C. Indeed, as shown in Fig. 21, oxide-scale cracking leads to the exposure of fresh bare metal to the oxidant at high temperature that can induce the growth of new transient oxides (i.e., γ-Al_2O_3). As the parabolic rate constant (k_p) for γ-Al_2O_3 growth is two orders of magnitude larger than for α-Al_2O_3, the mass gain can suddenly increase even if a small area is cracked. This also explains why γ-Al_2O_3 peaks reappeared on XRD of RT22/CMSX-4 after 27 and 35 cycles and of RT22/IN792 after 21 cycles (Figs. 11 and 13). SEM observation of RT22/IN792 surface after 35 cycles at 900°C (Fig. 22) confirms that new transient alumina forms close to cracks of the oxide scale.

Substrate Effect

Although the three superalloys were coated with the same coating RT22, prepared by the same company and under the same conditions, the initial oxidation kinetics are different. This was observed during ''short'' isothermal tests at 900–1150°C, but also during long-term cyclic oxidation at the lower temperature, 900°C. This effect essentially occurs during the transient stage and can be related to the initial chemical composition of the coating surface which depends on the protected superalloy chemistry and associated heat treatment.

First, it was observed for all samples that RT22 oxidizes faster on SCB than on CMSX4 and that IN792 is the substrate which leads to the lowest oxidation kinetics, at least during about 5000 h at 900°C (Fig. 10). This observation could be due to the effect of the reactive elements in the CMSX-4 alloy (Hf and Zr) and in the IN792 alloy (larger amounts of Hf and Zr), whereas SCB alloy has no reactive elements (Table I). Nevertheless, Zr and Hf were never detected during SEM–EDS and TEM–EDS analysis of the oxide scales. Moreover, these differences in mass gains are due mainly to initial oxidation (first two cycles), after which the oxidation kinetics are similar up to about 5000 h. But the substrate has another and perhaps more important effect. The Ni(Ti, Al, Ta)$_2$ phase detected on RT22/CMSX-4 leads to rutile/mixed-oxide formation which affects the oxidation kinetics during the transient stage, but also during long-term, cyclic-oxidation tests at 900°C. This substrate effect is due mainly to rutile oxide formed on RT22/CMSX-4 and on RT22/IN792 which causes oxide-scale cracking and re-oxidation of bare metal under these cracks. However, at 900°C, these systems have an excellent cyclic-oxidation behavior even for a very long duration test of 15,600 h. Then, such cyclic-oxidation tests at 900°C is not damaging enough to reach the lifetime of these superalloy/coating systems and to clearly show what system is the most resistant. At 900°C and below, corrosion is expected to be far more important than pure oxidation in a gas-turbine environment. Long-terms oxidation tests at 1050°C have been performed and reported in the second part of this paper.[43] At this higher temperature, interdiffusion between the coating and the substrate takes a large part in the damaging process[44] and is expected to have a large effect on cyclic-oxidation resistance.

CONCLUSIONS

Short-term, isothermal-oxidation tests at 900, 1050 and 1150°C and long-term, cyclic-oxidation tests at 900°C additionally to XRD and microstructural investigations were performed on the same Pt-modified, nickel-aluminide coating (RT22) on three different Ni-base superalloys (CMSX-4, SCB and IN792). From this study, several conclusions can be drawn:

1. a Ti,Ta-rich metallic phase was observed at the coating surface between β-NiAl grains in the RT22/CMSX-4 system. This phase leads to the formation of a rutile/mixed oxide (Al,Cr,Ti)(Ta,Ti)O_4 during the transient-oxidation stage, and a mechanism was proposed to explain the growth of this oxide.

2. The rutile oxide observed on RT22/IN792 does not form by the same mechanism as that on RT22/CMSX-4. This oxide is probably due to Ti diffusion from the substrate through the coating and the oxide scale up to the external surface where it can form TiO_2 above the existing alumina scale.
3. On RT22/SCB, because of a less pronounced thermal treatment which leads to a lower Ti content in the initial RT22 coating, no rutile oxide was detected after isothermal oxidation at 900 and 1050°C, and transformation of transient alumina θ-Al_2O_3 to α-Al_2O_3 is delayed compared to RT22/CMSX-4 and RT22/IN792. These observations suggest that Ti in the oxide scale accelerates the transformation of θ-Al_2O_3 into α-Al_2O_3. This may be related to the fact that Ti increases the densification rate and the final density of sintered α-Al_2O_3 from a δ-Al_2O_3 powder.[8]
4. Ti, Ta-rich oxide on RT22/CMSX-4 and RT22/IN792 appeared responsible for crack formation. This is either due to a much larger PBR ratio for TiO_2 than for Al_2O_3, leading to additional local compressive growth stresses and enhanced spalling during cooling, or because of the faster transformation of transient alumina to α-alumina. Indeed, a slow transformation with its associated molar volume reduction could be beneficial because of a reduction of the level of compressive stresses over a long period.
5. During long-term, cyclic-oxidation tests at 900°C, oxide-scale cracking induces the exposure of fresh bare metal to air and thus the formation of new transient oxides, increasing the mass gain for the RT22/CMSX-4 and RT22/IN792 systems.
6. At 900°C the substrate effect essentially occurs during the transient-oxidation stage because of the initial chemical composition of the coating surface which depends on the superalloys and associated heat treatments. The RT22/IN792 system has the slower oxidation kinetics up to 16 cycles of 300 h. This could be due to the presence of a significant amount of Hf and Zr in IN792, but these elements were never detected in the oxide scale. Nevertheless, the formation of the rutile layer on some systems has some negative consequences over a longer time.
7. The three systems tested have excellent long-term, cyclic-oxidation resistance at 900°C and are still far from their end of life after 15,60 h. Nevertheless, 900°C is an important temperature for gas-turbine applications. Then, these tests produce useful long-term cyclic-oxidation data that cannot be extrapolated from higher temperatures as the main degradation processes are different.

ACKNOWLEDGMENTS

The authors thank EEC for financial support through the European project Allbatros (NOENK5-CT2000-00081) and all partners for their contribution. Sincere thanks are expressed to Prof. B. Pieraggi for the fruitful discussions and helpful comments on the manuscript. Marie-Christine Lafont is acknowledged for the help in preparation of TEM samples and for the TEM observations.

REFERENCES

1. J. R. Nicholls, *MRS Bulletin* **9**, 659 (2003).
2. J. Angenete, and K. Stiller, *Material Science and Engineering* **A316**, 182 (2003).
3. J. Angenete, and K. Stiller, *Surface and Coatings Technology* **150**, 107 (2001).
4. M. Göbel, A. Rahmel, M. Schutze, M. Schorr, and W. T. Wu, *Materials at High Temperature* **12**, 301 (1994).
5. B. A. Pint, J. R. Martin, and L. W. Hobbs, *Solid State Ionics* **78**, 99 (1995).
6. V. K. Tolpygo, *Oxidation of Metals* **51**, 449 (1999).
7. D. Oquab, M.-C. Lafont, B. Viguier, D. Poquillon, and D. Monceau, *Materials Science Forum* **461–464**, 289 (2004).
8. S. Lartigue-Korinek, C. Legros, C. Carry, and F. Herbst, *Journal of the European Ceramic Society* **26**, 2219 (2006).
9. H. Hindam, and D. P. Whittle, *Oxidation of Metals* **18**, 245 (1982).
10. E. Schumann, J. C. Yang, M. J. Graham, and M. Ruehle, *Materials and Corrosion* **47**, 631 (1996).
11. B. A. Pint, J. R. Martin, and L. W. Hobbs, *Oxidation of Metals* **39**, 167 (1993).
12. E. W. Young, and J. H. W. d. Witt, *Solid State Ionics* **16**, 39 (1985).
13. B. A. Pint, *Electrochemical Society Extended Abstacts* **94–2**, 835 (1994).
14. H. E. Evans, *International Materials Reviews* **40**, 1 (1995).
15. V. K. Tolpygo, D. R. Clarke, and K. S. Murphy, *Metallurgical and Materials Transactions A* **32A**, 1467 (2001).
16. B. A. Pint, P. F. Tortorelli, and I. G. Wright, *Oxidation of Metals* **58**, 73 (2002).
17. N. Vialas, D. Monceau, and B. Pieraggi, *Materials Science Forum* **461–464**, 747 (2004).
18. B. Pint, I. Wright, W. Lee, Y. Zhang, K. Prübner, and K. Alexander, *Materials Science and Engineering A* **245A**, 201 (1998).
19. A. Littner, and M. Schütze, *JCSE* **6**, H023 (2003).
20. B. A. Pint, J. A. Haynes, K. L. More, I. G. Wright, C. Leyens, in *Superalloys* 2000, *TMS*, 629–638 (2000).
21. A. L. Purvis, and B. M. Warnes, *Surface and Coatings Technology* **146–1471**, 1 (2001).
22. A. El-Turki, G. C. Allen, C. M. Younes, and J. C. C. Day, *Materials Corrosion* **55**, 24 (2004).
23. M. J. Li, X. F. Sun, H. R. Guan, X. X. Jiang, and Z. Q. Hu, *Oxidation of Metals* **61**, 91 (2004).
24. P Caron, A. Escalé, G. McColvin, M. Blacker, R. Wahi, and L. Lelait, in *5th International Charles Parsons Turbine Conference*: Parsons 2000 Advanced Materials for 21st Century *Turbines and Power Plant*, Cambridge, UK, 03-07-00 (2000).
25. D. Monceau, and B. Pieraggi, *Oxidation of Metals* **50**, 477 (1998).
26. N. Vialas, phD thesis, Institut National Polytechnique de Toulouse (2004).
27. B. Huneau, P. Rogl, K. Zeng, R. Schmid-Fetzer, M. Bohn, and J. Bauer, *Intermetallics* **7**, 1337 (1999).
28. I. Ansara, and M. Selleby, *Calphad* **18**, 99 (1994).

29. Y. H. Zhang, D. M. Knowles, and P. J. Withers, *Surface and Coatings Technology* **107**, 76 (1998).
30. M. Durand-Charre, *The Microstructure of Superalloys* (Gordon and Breach Science Publishers, 1997), 124p.
31. M. W. Brumm, and H. J. Grabke, *Corrosion Science* **33**, 1677 (1992).
32. B. Gleeson, W. Wang, S. Hayashi, and D. Sordelet, *Materials Science Forum* **461–464**, 213 (2004).
33. J. Doychak, J. L. Smialek, and T. E. Mitchell, *Metallurgical and Materials Transactions A* **A20**, 499 (1989).
34. B. Pieraggi, and F. Dabosi, *Werkstoffe and korrosion* **38**, 575 (1987).
35. J. Angenete, Doctoral dissertation, Chalmers University of Technology Göteborg University (2002).
36. G. R. Krishna, D. K. Das, V. Singh, and S. V. Joshi, *Material Science and Engineering* **A251**, 40 (1998).
37. J. Benoist, K. F. Badawi, A. Mahlié, and C. Ramade, *Surface and Coatings Technology* **182**, 14 (2003).
38. D. K. Das, V. Singh, and S. V. Joshi, *Oxidation of Metals* **57**, 245 (2002).
39. B. Li, and B. Gleeson, *Oxidation of Metals* **62**, 45 (2004).
40. F. A. Grant, *Reviews of Modern Physics* **31**, 646 (1959).
41. N. Pilling, and R. Bedworth, *Journal of Instutition Metals* **29**, 529 (1923).
42. B. A. Pint, *Oxidation of Metals* **48**, 303 (1997).
43. N. Vialas, D. Monceau, *Oxidation of Metals*, Part II of this paper, submitted (2006).
44. N. Vialas, D. Monceau and B. Pieraggi, to be published (2006).